Chapter 13
High Resolution Kuroshio Forecast System: Description and its Applications

Takashi Kagimoto, Yasumasa Miyazawa, Xinyu Guo, and Hideyuki Kawajiri

Summary We have developed a forecast system for the Kuroshio large meander with a high horizontal resolution (approximately 10 km). Using the system, we succeeded in predicting the path transitions of the Kuroshio from the nearshore nonlarge meander path to the offshore nonlarge meander path in 2003, and from the nearshore nonlarge meander path to the typical large meander path in 2004 as well as the occurrence of its triggering small meander south of Kyushu Island. We have also been developing a higher resolution forecast model for coastal oceans and bays south of Japan, where physical and biological states of the ocean are much affected by the path variation of the Kuroshio. This model, although the development is still under way, represents tides and tidal currents in two bays south of Japan in a realistic way.

13.1 Introduction

The Kuroshio, one of the strongest surface currents in the world oceans, flows northeastward or eastward near Japan as a part of the subtropical gyre in the North Pacific. Because it carries enormous amounts of heat to the high latitude (e.g., 0.76 Peta Watt (PW) by Bryden et al.'s (1991) observation and 0.25–0.46 PW by Ichikawa and Chaen's (2000)), it plays a crucial role in maintaining and changing the global climate system. In particular the heat flux by the geostrophic advection of the Kuroshio has a substantial contribution to the local heat balance in the Kuroshio Extension region of the central North Pacific (Qiu and Kelly, 1993). Changes in the sea surface temperature associated with the Kuroshio path variations cause the surface wind to change (Nonaka and Xie, 2003), leading to some influence on the Pacific storm track (Inatsu et al., 2002). Thus in order to know climate variations in the North Pacific, it is important to grasp how the Kuroshio is and will be.

In addition the Kuroshio also affects coastal (local) areas because of its peculiar path variations. For example, the 100 m-depth temperature in Sagami Bay[1] is

[1] Reader may be unfamiliar to the names of those places. The locations of Enshu-nada Sea, Shikoku, Kyushu and Hachijo-jima Islands, and the Kii Peninsula are denoted by E, S, Q, H, and K, respectively, in the upper left panel of Fig. 13.6, that of Sagami Bay is by Sa in the left panel of Fig. 13.12, and that of the Izu Peninsula is in Fig. 13.14.

remarkably higher during the typical large meander path of the Kuroshio than other paths (Kawabe and Yoneno, 1987). The large meander of the Kuroshio may enhance the onshore intrusion of the warm water into the shelf region of the Enshu-nada Sea[1] and thereby contribute toward increasing the temperature in spawning habitats of sardine, leading to increase of postlarval sardine but to decrease of postlarval Japanese anchovy there (Nakata et al., 2000). Recent observations based on the long-term current measurements (Iwata and Matsuyama, 1989) and the HF radars (Hinata et al., 2005) indicate that the warm water intrusion into Sagami Bay is enhanced when the Kuroshio is located near the Izu Peninsula,[1] corresponding to either the nearshore nonlarge meander path or the typical large meander path. In addition to the physical and biological aspects, the location of the Kuroshio may have an influence on engineering activities such as the determination of optimal routes for ferries and cargo vessels. Thus the path variation of the Kuroshio is a general concern of many people as well as oceanographers.

In order to respond to their concerns it is necessary to predict the path variations of the Kuroshio. Several previous studies on development of a nowcast/forecast system for the Kuroshio have been accomplished. Komori et al. (2003) examine a capability for short-range forecast of the Kuroshio path variations south of Japan using a 1.5 layer primitive equation model with 1/12° resolution into which an objective analysis data of the sea surface height (Kuragano and Shibata, 1997) is assimilated with a variational method. The analysis fields obtained from the model are quite reasonable because the root-mean-square (RMS) differences with regard to the Kuroshio axis location south of the Enshu-nada Sea and the sea level at Hachijo-jima Island[1] between the reanalysis and the observations are less than the observed variances. The prediction errors are kept within the variances during 75-day prediction period, suggesting that the model has a predictability skill up to 75 days for the Kuroshio path variations. Ishikawa et al. (2004) point out, using the same forecast system, that an appropriate assimilation of a shoaling of the thermocline associated with a small meander of the Kuroshio south of Shikoku Island[1] into the model is of great importance in predicting the transition from the nearshore nonlarge meander path to the large meander path. Kamachi et al. (2004a) develop an operational ocean data assimilation system for the Kuroshio region using a more sophisticated ocean general circulation model with 1/4° resolution but with the simpler assimilation scheme of a time-retrospective nudging method than Komori et al.'s, and confirm that the reanalysis represents the real ocean reasonably well by comparing with individual observation data. The system, which has been operated in the Japan Meteorological Agency since January 2001, can predict the Kuroshio axis in 30- to 80-day prediction period in a manner that depends upon the ocean state in the initial condition (Kamachi et al., 2004b).

Previous studies have indicated several important factors in predicting the path transition of the Kuroshio: anticyclonic mesoscale eddies that appear in the subtropical frontal zone and move all the way to the south of Japan along the Kuroshio (Akitomo and Kurogi, 2001; Miyazawa et al., 2004), mesoscale eddies propagating westward from the Kuroshio Extension region to the southeast of Kyushu Island[1] (Ichikawa and Imawaki, 1994; Ebuchi and Hanawa, 2000; Akitomo and Kurogi,

2001; Mitsudera et al., 2001), the baroclinic instability process leading to the development of the small meander and the subsequent typical large meander (Endoh and Hibiya, 2000; Qiu and Miao, 2000), and a small seamount and associate abyssal circulation (Hurlburt et al., 1996; Endoh and Hibiya, 2000; Miyazawa et al., 2004). All of them suggest that numerical models are required to have a fine horizontal grid spacing so as to represent those factors reasonably well. Moreover, only a numerical model with a fine horizontal resolution can represent the realistic vertical structure of the velocity and the associated density structure in the Kuroshio region (Guo et al., 2003).

On the basis of the implications of previous studies, we developed a high resolution Kuroshio forecast system, called the Japan Coastal Ocean Predictability Experiment (JCOPE) ocean forecast system. The JCOPE project[2] has begun in October 1997 under an initiative of the Frontier Research Center for Global Change (FRCGC) / Japan Agency for Marine-Earth Science and Technology (JAMSTEC). As a part of the project, we have carried out fundamental simulation studies. Guo et al. (2003) examined effectiveness of a one-way nesting technique for the simulation of the Kuroshio. Miyazawa et al. (2004) pointed out the role of mesoscale eddies in the path variations of the Kuroshio using an eddy-resolving POM. Recently Miyazawa et al. (2005) indicated using a prototype of the forecast system that an initialization process with mesoscale eddies taken into account is crucial in predicting the path variations of the Kuroshio accurately. The present JCOPE forecast system finally reaches a stage of near-operational level using almost all available data obtained from satellites, ARGO (the Array for Real-time Geostrophic Oceanography) floats and ships, and its outcome is available on the Web site of the JCOPE project.[2] In this chapter we will describe details of the JCOPE ocean forecast system that is currently operated.

This chapter is organized as follows. In Sect. 13.2, we describe the numerical model, surface forcing data, and data assimilation scheme that we use for the forecast system in great detail. A couple of examples to show the forecast of the Kuroshio path transition are shown in Sect. 13.3. We also describe the sensitivity of the forecast to the parameters used in the data assimilation scheme. In Sect. 13.4, we briefly introduce our recent study toward downscaling of the Kuroshio forecast for coastal oceans and bays. Section 13.5 is devoted to summary and exemplification of some applications of the JCOPE outcome.

13.2 Description of Forecast System

13.2.1 Numerical Model

The numerical model that we adopt for the Kuroshio forecast system is a three-dimensional primitive-equation ocean general circulation model based on the POM with a generalized vertical coordinate (Mellor et al., 2002). The forecast system

[2] See `http://www.jamstec.go.jp/frcgc/jcope/`

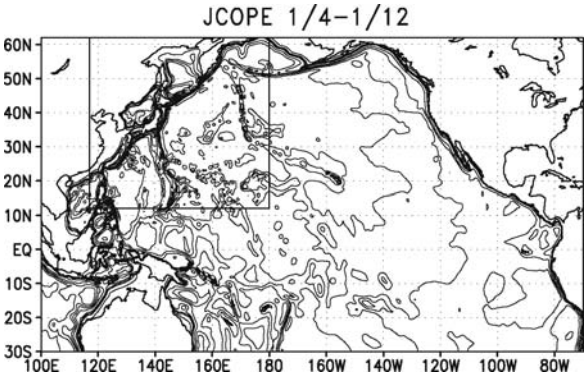

Fig. 13.1 Bottom topography used in the coarse model. Contour interval is 1,000 m. The small rectangle region delineated by solid straight lines is the computational domain for the fine model

consists of two models with different computational domains and resolutions: one is for the North Pacific basin with the variable horizontal resolution (1/4° near Japan and 1/2° in the east of basin) and 21 vertical levels; and the other is for the western North Pacific basin with 1/12° resolution and 45 levels (Fig. 13.1). The former model (hereafter coarse model) provides the boundary conditions for all prognostic variables described below to the latter (hereafter fine model), but the latter does not affect the former (no feedback).

The prognostic variables in the governing equations of the model are the surface elevation (η), the zonal and meridional components of the vertically averaged velocity ($\bar{u}$, $\bar{v}$), the zonal and meridional velocity (u, v), potential temperature (T), salinity (S), twice the turbulent kinetic energy (q^2), and turbulent length scale (l). A set of the equations for the latter two variables is a turbulent closure submodel (Mellor and Yamada, 1982), which is used for the estimation of the vertical eddy mixing coefficients. Mellor (2001) modified the treatment of the turbulent dissipation term in the submodel in such a way that the surface mixed layer did not become shallow overly in summer. With this correction Ezer (2000) succeeded in simulating the realistic vertical temperature profile in the North Atlantic, but Kagimoto (2003) pointed out that the correction caused overly mixing in the surface equatorial region where the vertical shear was strong and thereby the Equatorial Undercurrent almost disappeared. Hence we do not employ this modification. The horizontal eddy mixing coefficient is, on the other hand, evaluated by Smagorinsky's (1963) nonlinear formulation with constant coefficients of 0.1 for the coarse model and 0.075 for the fine model.[3] The coefficient for tracers is half of that for momentum, meaning that the turbulent Prandtl number is two.

The horizontal coordinate system is a conventional longitude–latitude grid, whereas the vertical one is a generalized "z-plus-sigma" grid. The depth of layer

[3] Those values correspond approximately to the so-called Smagorinsky's constants of 0.2659 and 0.23, respectively.

$1 \leq k \leq kb$ at location (x, y) and time t is defined by $z = \eta(x, y, t) + s(x, y, k, t)$, where kb is the number of vertical levels. A z-level system is $s^{(z)} = \sigma(k)[H_{\max} + \eta(x, y, t)]$, and a sigma coordinate system is $s^{(\sigma)} = \sigma(k)[H(x, y) + \eta(x, y, t)]$, where $H_{\max}$ is the maximum depth and the relative distribution of vertical layers is $0 \leq \sigma(k) \leq -1$ (Ezer and Mellor, 2004). In our formulation for the vertical grid, z-level grids are aligned on sigma grids. The boundary between the z-level system and the sigma-level system is located at k_e, the minimum value of indices that satisfy the following inequality,

$$|s^{(z)}(x, y, k_e, t)| > 0.5H(x, y) \tag{13.1}$$

Note that this formulation keeps surface layers from being over-resolved particularly in shallow areas (Mellor et al., 2002) and then prevents the sea surface temperature (SST) from being overestimated there. We also note that the bottom topography can be represented with the terrain following grid system more realistically than the z-level grids. In fact, the bottom relief is crucial to the representation of the Kuroshio because the bottom pressure torque plays a major role in the vorticity budget over the continental slope region at which the main axis of the Kuroshio is located (Kagimoto and Yamagata, 1997).

The bottom topography used in the model is based on the global DTM5 (Digital Terrain Models) with 1/12° resolution. For the fine model, the topography data with 500 m resolution archived by Hydrographic and Oceanographic Department, Japan Coastal Guard is also used for the area near Japan. In order to reduce the error in computing the pressure gradient force near steep topography, the topography data is smoothed out using two kinds of smoothing filters: the Gaussian smoothing with the 1/8° length scale, and the filter based on Mellor et al. (1994). The latter filter is continuously applied to the data until the depth satisfies the inequality $\delta H / \bar{H} \leq 0.35$, where δH is the depth difference between two neighboring grid points and $\bar{H}$ is the average depth between them. Note that the former filter is useful particularly for the variable grid system, which is adopted in our coarse model, because an effect of the filter that is not based on the local depth gradient but depth "difference" is inhomogeneous in space, thereby the bottom relief in areas with coarser resolutions is heavily smoothed out rather than with finer ones. The depths near the boundary of the fine model are calculated from the smoothed topography data used in the coarse model by using a bilinear interpolation in such a way that solutions of the fine model may be connected smoothly with those of the coarse model.

In the original POM, a partial slip condition is applied to the tangential component of the velocity at the boundary. We change it to the no-slip boundary condition, because the positive vorticity supply may be important to the development of the Kuroshio large meander (Akitomo et al., 1991). The temperature and salinity near the artificial boundaries in the coarse model are restored to the monthly mean climatology (Levitus and Boyer, 1994; Levitus et al., 1994) in such a way that fictitious waves neither propagate along nor reflect at the boundaries. Since sea ice processes are not taken into account in the forecast system, both the temperature and salinity of the coarse model in the Sea of Okhotsk and the Bering Sea are also restored to the

monthly mean climatology. In the fine model, they are restored to the climatology only in the Sea of Okhotsk.

The initial condition is a state of rest with the 1/4° annual mean climatological temperature and salinity fields (Boyer and Levitus, 1997). The coarse model is spun up for 10 years from the initial state with the use of the monthly mean surface forcings described below. Then it is further driven by 6 hourly surface forcings covering from September 1999 to December 2001. The fine model is also forced from the initial state with the monthly mean surface forcings but for 5 years, and is continued to be forced with the 6 hourly forcings from September 1999 to December 2001. The data assimilation scheme described in Sects. 13.2.5 and 13.2.7 is introduced from September 1999. Then the forecast experiment together with the data assimilation is started in December 2001.

13.2.2 Nesting

As described earlier, the coarse model provides the boundary values of the prognostic variables to the fine model. All prognostic variables except for two turbulent properties in the coarse model are linearly interpolated on to the boundary grid points of the fine model. In order to reduce noise caused by a mismatch between two models, we modify the vertically averaged velocity normal to the boundary with the use of the following radiation condition (Flather, 1976; Guo et al., 2003),

$$\bar{u}_{\mathrm{f}} = \bar{u}_{\mathrm{c}} - c_{\mathrm{rf}}\sqrt{\frac{g}{H}}(\eta_{\mathrm{f}} - \eta_{\mathrm{c}}) \tag{13.2}$$

where $\bar{u}_{\mathrm{c}}$ and η_{c} are, respectively, the interpolated values of the normal component of the velocity and the surface elevation, g is the gravity constant, η_{f} is the surface elevation of the fine model at a grid inside the open boundary, and c_{rf} is an adjustable parameter ($0 < c_{\mathrm{rf}} \leq 1$), for which we select 0.1. The turbulent properties, q^2 and $q^2 l$, are set to be a constant of 10^{-10}, meaning that the turbulent energy advected from the outside is ignored.

13.2.3 Surface Forcings

The zonal and meridional components of the momentum flux (τ_x, τ_y) are parameterized with the following bulk formula,

$$(\tau_{\mathrm{x}}, \tau_{\mathrm{y}}) = \rho_{\mathrm{a}} C_{\mathrm{D}} \sqrt{u_{10\mathrm{m}}^2 + v_{10\mathrm{m}}^2}(u_{10\mathrm{m}}, v_{10\mathrm{m}}) \tag{13.3}$$

where $\rho_{\mathrm{a}} = 1.225\ \mathrm{kg\,m^{-3}}$ is the air density at sea level, $u_{10\mathrm{m}}$ and $v_{10\,\mathrm{m}}$ are, respectively, the zonal and meridional components of wind velocity at 10 m above sea level

($\mathrm{m\,s^{-1}}$), and C_D is the drag coefficient based on Large and Pond's (1981) formula, that is,

$$10^3 \times C_\mathrm{D} = \begin{cases} 1.14, & (\sqrt{u_{10\mathrm{m}}^2 + v_{10\mathrm{m}}^2} < 10) \\ 0.49 + 0.067\sqrt{u_{10\mathrm{m}}^2 + v_{10\mathrm{m}}^2}, & (10 \le \sqrt{u_{10\mathrm{m}}^2 + v_{10\mathrm{m}}^2} < 26) \\ 0.49 + 0.065 \times 26, & (26 \le \sqrt{u_{10\mathrm{m}}^2 + v_{10\mathrm{m}}^2}) \end{cases} \quad (13.4)$$

For $u_{10\mathrm{m}}$ and $v_{10\mathrm{m}}$, we adopt the QuikSCAT Near-Realtime data products (Liu et al., 1998), whose spatial and temporal resolutions are half a degree and 12 h, respectively. Although the resolutions are coarser than the intrinsic ones in the NASA/JPL's Sea-Winds Scatterometer, the products have the advantage of less sampling error along the satellite track than others.

The turbulent heat flux $\overline{w'T'}$ is evaluated using the following equation,

$$\rho_\mathrm{a} C_\mathrm{p} \overline{w'T'} = (Q_\mathrm{L} + Q_\mathrm{E} + Q_\mathrm{H}) - \frac{dQ}{dT}(T_\mathrm{s} - T_\mathrm{obs}) \quad (13.5)$$

where $C_\mathrm{p} = 1.005 \times 10^3\,\mathrm{J\,kg^{-1}\,K^{-1}}$ is the specific heat capacity, Q_L is the long-wave radiation, Q_E is the latent heat flux, Q_H is the sensible heat flux, $\mathrm{d}Q/\mathrm{d}T = -35\,\mathrm{W\,m^{-2}\,K^{-1}}$ is the coupling coefficient, and T_s and T_obs are the model and observed SST, respectively. The last term of (13.5) is the correction term to reduce SST biases. The first three terms are parameterized with the bulk formulas,

$$Q_\mathrm{L} = \epsilon\sigma T_\mathrm{obs}^4(0.39 - 0.05\sqrt{e_\mathrm{a}})(1 - 0.8C) + 4\epsilon\sigma T_\mathrm{obs}^3(T_\mathrm{obs} - T_\mathrm{a}) \quad (13.6)$$

$$Q_\mathrm{E} = \rho_\mathrm{a} C_\mathrm{E} L\sqrt{u_{2\mathrm{m}}^2 + v_{2\mathrm{m}}^2}(q_\mathrm{sat}(T_\mathrm{obs}) - q_\mathrm{a}) \quad (13.7)$$

$$Q_\mathrm{H} = \rho_\mathrm{a} C_\mathrm{p} C_\mathrm{H}\sqrt{u_{2\mathrm{m}}^2 + v_{2\mathrm{m}}^2}(T_\mathrm{obs} - T_\mathrm{a}) \quad (13.8)$$

where $\epsilon = 0.97$ is the emissivity of the ocean, $\sigma = 5.67 \times 10^{-8}\,\mathrm{W\,m^{-2}\,K^{-4}}$ is the Stefan-Boltzmann constant, C is the fraction cloud cover, T_a is the air temperature, $L = 2.501 \times 10^6\,\mathrm{J\,kg^{-1}}$ is the latent heat of fusion, $q_\mathrm{sat}(T_\mathrm{obs})$ is the saturated specific humidity at T_obs, and q_a is the specific humidity. The saturated specific humidity is related to the saturated vapor pressure, which is approximately a polynomial function of temperature (Tetens, 1930). The vapor pressure, e_a, is calculated from q_a using the same relationship. The zonal and meridional wind velocities at 2 m above sea level, $(u_{2\mathrm{m}}, v_{2\mathrm{m}})$, are estimated from $u_{10\mathrm{m}}$ and $v_{10\mathrm{m}}$ using the logarithmic law. The turbulent exchange coefficients, C_E and C_H, are based on Kondo's (1975) formulas.

The incoming shortwave radiation at the sea surface, Q_s, is estimated with an empirical formula,

$$Q_\mathrm{s} = Q_\mathrm{s}^\mathrm{sky}(0.77 - 0.5C^2)(1 - \alpha) \quad (13.9)$$

where $Q_\mathrm{s}^\mathrm{sky}$ is the solar radiation incident on the ocean under clear skies, and $\alpha = 0.08$ is the ocean surface albedo. Equation (13.9) is different from numer-ous empirical relations proposed in previous studies (e.g., Reed, 1977). The factor,

$(0.77 - 0.5C^2)$, is found out with trial and error in such a way that the climatological model SST becomes close to the observed one. The penetration of the shortwave radiation into the ocean is taken into account on the basis of Paulson and Simpson's (1977) formulation,

$$I(z) = Q_s \left(\gamma \exp\left(\frac{z}{\zeta_1}\right) + (1-\gamma) \exp\left(\frac{z}{\zeta_2}\right) \right) \tag{13.10}$$

where $I(z)$ is the penetrated solar radiation flux at depth z, ζ_1 and ζ_2 are, respectively, the e-folding depths of the long (ζ_1), and short visible and ultra violet (ζ_2) wavelengths, and γ is a fraction for the former part. We select $\gamma = 0.58$, $\zeta_1 = 0.35\,\mathrm{m}$, and $\zeta_2 = 23.0\,\mathrm{m}$, corresponding to the type I water of Jerlov's (1976) classification.[4]

Those fluxes require the observed SST, surface air temperature, specific humidity, the fraction cloud cover, and the solar radiation incident on the ocean under clear skies. We adopt the 6 hourly NCEP/NCAR reanalysis product (Kalnay et al., 1996) for them.

The sea surface salinity, S_s, is restored to the monthly climatology (Levitus et al., 1994), S_{obs}, in the form of the salinity flux,

$$\overline{w's'} = \gamma_s (S_s - S_{obs}) \tag{13.11}$$

where $\gamma_s = 10\,\mathrm{m\,month^{-1}}$ is the restoring speed.

13.2.4 Observational Data

The observations assimilated into the model are the satellite altimeter data obtained from the TOPEX/POSEIDON and ERS-1 during September 1999 to June 2002 and from the Jason-1 and the GeoSat Follow-On during June 2002 to the present, the sea surface temperature from the advanced very high resolution radiometer/multichannel sea surface temperature (AVHRR/MCSST) Level 2 products, and vertical profile data of the temperature and salinity provided by the Global Temperature-Salinity Profile Program (GTSPP). From these data, we build up 7 days interval data on 1/4° grids using the optimal interpolation technique described later. The sampling period for the satellite data is 7 days (before and after 3 days of an analysis time), while that for the temperature and salinity profile is 31 days. The spatial extent of sampling data is 360 km.

The gridded anomaly of a variable, a_g, is calculated using a linear combination of the observed anomaly of the variable, a_o,

$$a_g = W^T a_o \tag{13.12}$$

[4] The type II or IA is better for the water off Japan, but the use of the e-folding depths corresponding to the waters resulted in a warm bias of the SST. Hence we chose the type I water.

where a_g and a_o are, respectively, the column vectors with N and M elements, W is a $M \times N$ matrix of weights,[5] M is the number of observation points, and N is the number of grid points. The superscript of W, T, denotes the transpose of the matrix. The matrix, W, is found by minimizing the variance of interpolation errors, and obtained from solving the algebraic equation (Gandin, 1963),

$$(P^{oo} + \lambda I)W = P^{og} \tag{13.13}$$

where I is the unit matrix. The $M \times M$ matrix of the autocorrelation of the observed values, P^{oo}, is parameterized with a Gaussian model,

$$\begin{aligned} P^{oo} &= (P^{oo}_{i,j}) \\ &= P^{oo}(\boldsymbol{x}_i; \boldsymbol{x}_j) \\ &= C_0(x_i, y_i, z_i) \exp\left(-\left(\frac{\Delta x - c_x \Delta t}{L_x}\right)^2 - \left(\frac{\Delta y}{L_y}\right)^2 - \left(\frac{\Delta t}{L_t}\right)^2\right) \end{aligned} \tag{13.14}$$

where $\boldsymbol{x}_i = (x_i, y_i, z_i, t_i)$ and $\boldsymbol{x}_j$ are two observation points, C_0 is the autocorrelation at lag 0, $\Delta x = x_i - x_j$, $\Delta y = y_i - y_j$, $\Delta t = t_i - t_j$, c_x is a phase speed in the zonal direction, and L_x, L_y, and L_t, respectively, denote the zonal, meridional, and temporal decorrelation scales. The $M \times N$ matrix of the autocorrelation between the observed and interpolated values, P^{og}, is also calculated from (13.14), but $\boldsymbol{x}_j$ is replaced with $\boldsymbol{x}_g$, which denotes a grid point to which the data are interpolated. The signal-to-noise ratio, λ in (13.13), is calculated with C_0,

$$\lambda = \frac{1 - C_0}{C_0} \tag{13.15}$$

The parameters, C_0, L_x, L_y, L_t, and c_x, required by the optimal interpolation are calculated from the following procedures using the observation data listed in Table 13.1.

1. Create a mean field during a period
2. Calculate the autocorrelation at observation points and average the correlation matrices within $5^\circ \times 5^\circ$ regions

Table 13.1 Data used to estimate the parameters in (13.14)

Data	Instruments	Distributor	Period	Mean
SSH	TOPEX/POSEIDON, ERS-2	CCAR	Sep 1999–Jun 2002	None
SST	AVHRR	JPL, NAVO-CEANO	Oct 2001–Aug 2002	Mean during the period
T & S (0–400 m)	CTD, XBT, MBT, etc.	GTSPP	Mar 1990–Mar 2002	Boyer and Levitus (1997)

[5] For the sake of convenience, (13.12) is expressed with the matrix form, but in the numerical calculation W is evaluated at each grid point. Thus in practice a_g is a scalar, W is an M elements column vector.

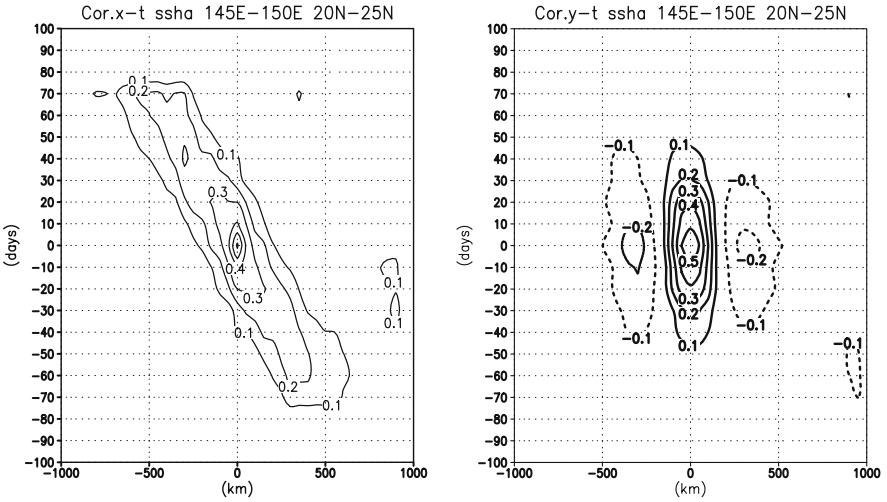

Fig. 13.2 Autocorrelation of the sea surface height (SSH) anomaly in the region, 20°N–25°N, 145°E–150°E. (*Left*) Time-longitude lag-correlation. (*Right*) Time-latitude lag-correlation. Contour interval is 0.1. *Solid line* denotes positive values and *dashed line* denotes negative values

3. Estimate the parameters by fitting the Gaussian model described earlier
4. Interpolate/extrapolate the parameters on to 1/4° grids
5. Smooth out the parameters using the Gaussian filter with 3° horizontal scale

Figure 13.2 shows an example of the autocorrelation of the sea surface height (SSH) anomaly based on the altimetry data in the region, 20°N–25°N, 145°E–150°E, obtained from procedure 2. By fitting the autocorrelation, in a least square sense, to the Gaussian model of (13.14) (procedure 3), we obtain the parameters,

$$(C_0,\, c_x,\, L_x,\, L_y,\, L_t) = (0.626,\, -0.07\ \mathrm{m\,s^{-1}},\, 152\,\mathrm{km},\, 108\,\mathrm{km},\, 53\,\mathrm{days}) \quad (13.16)$$

The approximate autocorrelation function with the above parameters is shown in Fig. 13.3. Both the time-longitude and time-latitude correlation functions are good approximations, although the negative correlation at 300 km apart from the specific point is not represented in the latter (right panels of Figs. 13.2 and 13.3).

13.2.5 Data Assimilation

The SSH anomaly, $\tilde{\eta}^o$, and the vertical profile of the temperature and salinity, $T^o(z_1)$, $T^o(z_2)$, $\cdots$, $T^o(z_M)$, $S^o(z_1)$, $S^o(z_2)$, $\cdots$, $S^o(z_M)$, gridded in the way described in the previous subsection are combined with a forecast data, leading to an analysis data on the 1/12°horizontal grids and the "z-plus-sigma" vertical grids, which is used for the increment analysis update (IAU) process described in Sect. 13.2.7. In our

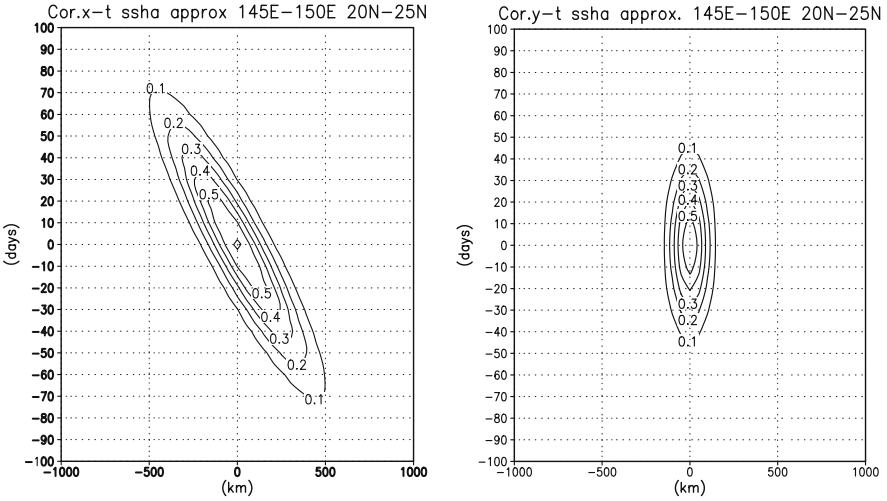

Fig. 13.3 Approximate autocorrelation function of the SSH anomaly in the region, 20°N–25°N, 145°E–150°E fitted to the Gaussian model, (13.14). (*Left*) Time-longitude lag-correlation. (*Right*) Time-latitude lag-correlation. Contour interval is 0.1

system, the number of vertical levels for the gridded observation data, M, is 6, and the corresponding depths, $z_k (k = 1, \cdots, M)$, are 0, 50, 100, 200, 300, and 400 m.

For the data assimilation process, we use a multivariate optimal interpolation scheme described later (Lorenc, 1981; Ezer and Mellor, 1997). Before the interpolation, we subtract basin-wide seasonal variations such as the thermal expansion from the SSH anomaly, that is,

$$\tilde{\eta}' = \tilde{\eta} - \sum_{\text{latitude}} \tilde{\eta} \tag{13.17}$$

This enables us to assimilate the data of the SSH variations associated with mesoscale eddies effectively into the model (Y. Wakata, personal comm., 1999).

Define the analysis state, X^{a}, as a $2N + 1$ elements column vector,

$$X^{\mathrm{a}} = (\tilde{\eta}'^{\mathrm{a}}, T_1^{\mathrm{a}}, T_2^{\mathrm{a}}, \cdots, T_{\mathrm{N}}^{\mathrm{a}}, S_1^{\mathrm{a}}, S_2^{\mathrm{a}}, \cdots, S_{\mathrm{N}}^{\mathrm{a}}) \tag{13.18}$$

where N denotes the number of vertical "z-plus-sigma" levels. The forecast state, X^{f}, and the observation value, y^{o}, are also defined in the same way,

$$X^{\mathrm{f}} = (\tilde{\eta}'^{\mathrm{f}}, T_1^{\mathrm{f}}, T_2^{\mathrm{f}}, \cdots, T_{\mathrm{N}}^{\mathrm{f}}, S_1^{\mathrm{f}}, S_2^{\mathrm{f}}, \cdots, S_{\mathrm{N}}^{\mathrm{f}}) \tag{13.19}$$

$$y^{\mathrm{o}} = (\tilde{\eta}'^{\mathrm{o}}, T_1^{\mathrm{o}}, T_2^{\mathrm{o}}, \cdots, T_{\mathrm{M}}^{\mathrm{o}}, S_1^{\mathrm{o}}, S_2^{\mathrm{o}}, \cdots, S_{\mathrm{M}}^{\mathrm{o}}) \tag{13.20}$$

The analysis state is calculated from the best linear invariant estimation,

$$X^{\mathrm{a}} = X^{\mathrm{f}} + PH^{\mathrm{T}}(HPH^{\mathrm{T}} + R)^{-1}(y^{\mathrm{o}} - HX^{\mathrm{f}}) \tag{13.21}$$

where P is the error covariance matrix of the forecast state with $(2N+1) \times (2N+1)$ elements, H is the observation matrix with $(2M + 1) \times (2N + 1)$ elements that

is a linear operator mapping the forecast state into the observed data, and R is the observation error covariance matrix with $(2M+1)\times(2M+1)$ elements. The Kalman gain matrix, $PH^{\mathrm{T}}(HPH^{\mathrm{T}}+R)^{-1}$, acts as interpolation and/or extrapolation of the innovation, $y^{\mathrm{o}}-HX^{\mathrm{f}}$, to the model state. The error covariance matrix is the function of time and space that depends upon the model physics. For simplicity, however, we assume it to be constant in time, and estimate it in advance.

Suppose, for a simple explanation, that $M=N=1$. In this case, the observation matrix becomes the 3×3 unit matrix, and the matrix, PH^{T} is expressed as follows,

$$PH^{\mathrm{T}}=\begin{pmatrix} \langle(\delta\tilde{\eta}'^{\mathrm{f}})^2\rangle & \langle\delta\tilde{\eta}'^{\mathrm{f}}\delta T^{\mathrm{f}}\rangle & \langle\delta\tilde{\eta}'^{\mathrm{f}}\delta S^{\mathrm{f}}\rangle \\ \langle\delta T^{\mathrm{f}}\delta\tilde{\eta}'^{\mathrm{f}}\rangle & \langle(\delta T^{\mathrm{f}})^2\rangle & \langle\delta T^{\mathrm{f}}\delta S^{\mathrm{f}}\rangle \\ \langle\delta S^{\mathrm{f}}\delta\tilde{\eta}'^{\mathrm{f}}\rangle & \langle\delta S^{\mathrm{f}}\delta T^{\mathrm{f}}\rangle & \langle(\delta S^{\mathrm{f}})^2\rangle \end{pmatrix} \tag{13.22}$$

where δx and $\langle x\rangle$ denote, respectively, the error and expectation of a variable, x. Assuming that each element of the matrix, PH^{T}, can be approximately estimated from the variance of the variables obtained from the model (Mellor and Ezer, 1991).

$$\begin{aligned} PH^{\mathrm{T}} &\approx \begin{pmatrix} \overline{(\Delta\tilde{\eta}'^{\mathrm{f}})^2}E^{\mathrm{f}}_{\eta'} & \overline{\Delta\tilde{\eta}'^{\mathrm{f}}\Delta T^{\mathrm{f}}}E^{\mathrm{f}}_{T} & \overline{\Delta\tilde{\eta}'^{\mathrm{f}}\Delta S^{\mathrm{f}}}E^{\mathrm{f}}_{S} \\ \overline{\Delta T^{\mathrm{f}}\Delta\tilde{\eta}'^{\mathrm{f}}}E^{\mathrm{f}}_{\eta'} & \overline{(\Delta T^{\mathrm{f}})^2}E^{\mathrm{f}}_{T} & \overline{\Delta T^{\mathrm{f}}\Delta S^{\mathrm{f}}}E^{\mathrm{f}}_{S} \\ \overline{\Delta S^{\mathrm{f}}\Delta\tilde{\eta}'^{\mathrm{f}}}E^{\mathrm{f}}_{\eta'} & \overline{\Delta S^{\mathrm{f}}\Delta T^{\mathrm{f}}}E^{\mathrm{f}}_{T} & \overline{(\Delta S^{\mathrm{f}})^2}E^{\mathrm{f}}_{S} \end{pmatrix} \\ &= \begin{pmatrix} 1 & F_{\eta' T} & F_{\eta' S} \\ F_{T\eta'} & 1 & F_{TS} \\ F_{S\eta'} & F_{ST} & 1 \end{pmatrix} \begin{pmatrix} E^{\mathrm{f}}_{\eta'} & 0 & 0 \\ 0 & E^{\mathrm{f}}_{T} & 0 \\ 0 & 0 & E^{\mathrm{f}}_{S} \end{pmatrix} \\ &\quad\times \begin{pmatrix} \overline{(\Delta\tilde{\eta}'^{\mathrm{f}})^2} & 0 & 0 \\ 0 & \overline{(\Delta T^{\mathrm{f}})^2} & 0 \\ 0 & 0 & \overline{(\Delta S^{\mathrm{f}})^2} \end{pmatrix} \end{aligned} \tag{13.23}$$

where $\overline{x}$ and Δx denote the time mean of a variable, x, and the deviation from it, respectively. The regression coefficient between variables, x and y, denoted by F_{xy}, is expressed as follows,

$$F_{xy}=\frac{\overline{\Delta x\Delta y}}{\overline{\Delta y^2}} \tag{13.24}$$

In this way, the estimation of the forecast error covariance matrix results in the estimation of the nondimensional parameters, $E^{\mathrm{f}}_{\eta'}$, $E^{\mathrm{f}}_{\mathrm{T}}$, and $E^{\mathrm{f}}_{\mathrm{S}}$, which are the forecast error variances normalized by the variances in the forecast data. Note that the spatial pattern of the regression coefficients depends strongly upon the model performance, suggesting that the improvement of the model performance is crucial to refinement of the regression coefficients.

Assuming that an observation error of a variable is not correlated to that of another, R becomes a diagonal matrix,

$$R\approx \begin{pmatrix} E^{\mathrm{o}}_{\eta'} & 0 & 0 \\ 0 & E^{\mathrm{o}}_{\mathrm{T}} & 0 \\ 0 & 0 & E^{\mathrm{o}}_{\mathrm{S}} \end{pmatrix} \begin{pmatrix} \overline{(\Delta\tilde{\eta}'^{\mathrm{f}})^2} & 0 & 0 \\ 0 & \overline{(\Delta T^{\mathrm{f}})^2} & 0 \\ 0 & 0 & \overline{(\Delta S^{\mathrm{f}})^2} \end{pmatrix} \tag{13.25}$$

where $E^{\mathrm{o}}_{\eta'}$, $E^{\mathrm{o}}_{\mathrm{T}}$, and $E^{\mathrm{o}}_{\mathrm{S}}$ are the observation error variances normalized by the variances in the forecast data.

If the probability distributions of the observation and forecast errors are independent of each other, we obtain the innovation covariance matrix,

$$\langle (y^{\mathrm{o}} - HX^{\mathrm{f}})(y^{\mathrm{o}} - HX^{\mathrm{f}})^{\mathrm{T}} \rangle = HPH^{\mathrm{T}} + R \tag{13.26}$$

Comparison of the diagonal components between both sides of (13.26) gives a simple relation of the observation and forecast errors to the model statistics for each variable,

$$\begin{aligned} (E^{\mathrm{f}}_{\eta'} + E^{\mathrm{o}}_{\eta'})\langle(\Delta\tilde{\eta}'^{\mathrm{f}})^2\rangle &= \langle(\tilde{\eta}'^{\mathrm{f}} - \tilde{\eta}'^{\mathrm{o}})^2\rangle \\ (E^{\mathrm{f}}_{\mathrm{T}} + E^{\mathrm{o}}_{\mathrm{T}})\langle(\Delta T^{\mathrm{f}})^2\rangle &= \langle(T^{\mathrm{f}} - T^{\mathrm{o}})^2\rangle \\ (E^{\mathrm{f}}_{\mathrm{S}} + E^{\mathrm{o}}_{\mathrm{S}})\langle(\Delta S^{\mathrm{f}})^2\rangle &= \langle(S^{\mathrm{f}} - S^{\mathrm{o}})^2\rangle \end{aligned} \tag{13.27}$$

Thus the amplitude of the observation and forecast errors are not determined independently, but the ratio between them is. Note that the ratio strongly affects forecast skills, because when $E^{\mathrm{o}}_{\mathrm{x}}$ is bigger (smaller) than $E^{\mathrm{f}}_{\mathrm{x}}$ the forecast (observation) data are set above the observation (forecast) in determining the analysis data used in the IAU process described in Sect. 13.2.7. In fact we realize that the prediction of the Kuroshio large meander is sensitive particularly to the error ratio associated with the SSH anomaly. Now we introduce an adaptive assimilation scheme (Fox et al., 2000) in order to estimate the adequate forecast error variance in (13.27),[6]

$$\begin{aligned} E^{\mathrm{f}}_{\eta'} G[\langle(\Delta\tilde{\eta}'^{\mathrm{f}})^2\rangle] &= G[\langle(\tilde{\eta}'^{\mathrm{f}} - \tilde{\eta}'^{o})^2\rangle - \alpha_{\eta'} e_i^2(\tilde{\eta}^o)] \\ E^{o}_{\eta'} G[\langle(\Delta\tilde{\eta}'^{\mathrm{f}})^2\rangle] &= G[\alpha_{\eta'} e_i^2(\tilde{\eta}^o)] \end{aligned} \tag{13.28}$$

$$\begin{aligned} E^{\mathrm{f}}_{\mathrm{T}_0} G[\langle(\Delta T_0^{\mathrm{f}})^2\rangle] &= G[\langle(T_0^{\mathrm{f}} - T_0^{o})^2\rangle - \alpha_{\mathrm{T}_0} e_i^2(T_0^o)] \\ E^{o}_{\mathrm{T}_0} G[\langle(\Delta T_0^{\mathrm{f}})^2\rangle] &= G[\alpha_{\mathrm{T}_0} e_i^2(T_0^o)] \end{aligned} \tag{13.29}$$

where $G[\cdot]$ is the spatial filter of the Gaussian shape with a zonal scale of 1.4° (the equator)–0.7° (60°N) and a meridional scale of 0.4° (the equator)–0.2° (60°N), and T_0 is the SST. The interpolation error covariance of a variable x, $e_i^2(x)$, is defined by

$$e_i^2 = V_{\mathrm{s}}^2 (1 - W^T P^{\mathrm{og}}) \tag{13.30}$$

where V_{s}^2 is a signal variance of the variable. The difference between the original adaptive assimilation scheme proposed by Fox et al. (2000) and ours is the existence of the adjustable parameters, $\alpha_{\eta'}$ and α_{T_0}, which are found out from the sensitivity experiments in such a way that the predicted Kuroshio large meander is as close to the observation as possible. If there are sufficient data to interpolate on to the model grids, α_x should be unity. In our case, however, the amount of satellite data is insufficient particularly on the onshore side of the Kuroshio, and then the interpolation error

[6] Because the satellite data has much information due to high spatio-temporal resolutions, the error variances of the SSH and SST obtained from the adaptive assimilation scheme are more reliable than those of the temperature and salinity from hydrographic observations. Hence we apply the scheme to the SSH and SST data, although the forecast is not so sensitive to the choice of the SST error variance.

covariance has a large uncertainty. Hence we introduce the adjustable parameter in (13.28) and (13.29). Note that there is a constraint on the sensitivity experiments. Since the distribution of the following variable,

$$(y^{\mathrm{o}} - HX^{\mathrm{f}})^{\mathrm{T}}(HPH^{\mathrm{T}} + R)^{-1}(y^{\mathrm{o}} - HX^{\mathrm{f}})$$

asymptotically approaches to the normal distribution with mean M and variance $2M$, as M goes to infinity (Lupton, 1993), we need to confirm that the sum of the above variable over the computational domain is close to the unity (Menard and Chang, 2000),

$$\frac{1}{LM}\sum_{i=1}^{L}(y_i^{\mathrm{o}} - HX_i^{\mathrm{f}})^{\mathrm{T}}(HP_iH^{\mathrm{T}} + R_i)^{-1}(y_i^{\mathrm{o}} - HX_i^{\mathrm{f}}) \approx 1 \tag{13.31}$$

where L is the number of horizontal grid points.

Several parameters listed in Table 13.2 are introduced into the data assimilation scheme described above. The adaptive assimilation scheme is applied only in the Kuroshio region of `isadpt` $\leq$ longitude $\leq$ `ieadpt` and `jsadpt` $\leq$ latitude $\leq$ `jeadpt`, because our main target to predict is the Kuroshio path variations. Hence the normalized error variances for the SSH and SST out of the region are set to be constants. Those for the temperature below the surface and the salinity are also assumed to be constants because their effect on the forecast skill is not so large. The values of E_x^{o} and E_x^{f} for a variable x are, respectively, listed in the lines of `vobsadj0` and `vmodeladj0` of Table 13.2. The parameter, `vobsieadj`, corresponds to α_x for a variable x.

The data assimilation (the estimation of the analysis values) does not take place in the whole of the computational domain. If the depth at a grid point is out of range of `hup` to `hlow` or less than `hassim`, the observation data is not assimilated, that is, the Kalman gain in (13.21) is set to be zero. The parameter, `vobsiemax0`, is

Table 13.2 Parameters used for the data assimilation

Parameters	SSH	SST	T	S
`hup`	0 m	0 m	50 m	0 m
`hlow`	3 000 m	200 m	3 000 m	3 000 m
`hassim`	200 m	10 m	50 m	10 m
`vobsiemax0`	0.9	0.9	0.8 [7]	0.8 [7]
`vobsadj0`	0.48	0.01	0.192	0.192
`vmodeladj0`	0.036	0.01	0.048	0.048
`vcorimpt`	1.0	1.0	1.0	0.0
`vcorimps`	0.1	0.0	0.0	1.0
`isadpt`	117°E	117°E	-	-
`ieadpt`	141°E	180°E	-	-
`jsadpt`	12°N	12°N	-	-
`jeadpt`	44°N	62°N	-	-
`vobsieadj`	0.6	1.0	-	-

[7] The value of 0.6 is used for the temperature at 50 and 100 m and the salinity at 0, 50, and 100 m.

the acceptable maximum interpolation error, implying that if e_i / V_s is larger than the value the observation data is not assimilated. Additionally all data except for the SST are not unconditionally assimilated in the region of 117°E to 180° and 44°N to 62°N. In fact the data assimilation in this area is not significant, partly because the temperature and salinity are restored to the monthly mean climatology in the Okhotsk Sea described in Sect. 13.2.1, partly because the number of hydrographic observation data in the northern North Pacific is quite few, and partly because the relationship between the SSH anomaly and the in-situ temperature and salinity is unclear there, meaning that the regression coefficient is small.

In the data assimilation process, the regression coefficients between the temperature at the depth k and a variable x, $F_{\mathrm{T}_k x}$, and between the salinity at the depth k and the variable, $F_{\mathrm{S}_k x}$, are factorized by the adjustable parameters, `vcorimpt` and `vcorimps`, respectively, because we realize that the forecast skill got worse when the temperature and salinity are assimilated with the same weight as each other. These parameters are empirically determined.

13.2.6 Quality Control

Both the raw and gridded data of the observation are quality controlled in a simple way. They are required to be within the range of `valmin` to `valmax`, and the absolute value of their anomaly to be less than `valamax`. If the data value is out of range, it is converted to be a missing value. Even if within the range, the raw data at the depth shallower than `hobsmin` are excluded in the optimal interpolation process. Additionally the gridded data at the depth shallower than `hmin` are discarded before the subsequent multivariate optimal interpolation process is carried out. The exclusion process is due to the worse accuracy of the satellite altimetry data particularly in shallow coastal areas and marginal seas than in open oceans. The parameters used in the data quality control process for each variable are listed in Table 13.3.

The analysis data obtained from the multivariate optimal interpolation scheme is also quality controlled. The analysis value of the temperature, T^{a}, and the salinity, S^{a}, is required to be within the range,

$$|T^{\mathrm{a}} - T^{\mathrm{f}}| \leq 8, \quad -1 \leq T^{\mathrm{a}} \leq 32 \tag{13.32}$$

Table 13.3 Parameter values for the data quality control

	SSH	SST	T	S
`hmin`	200 m	10 m	10 m	10 m
`hobsmin`	100 m	10 m	10 m	10 m
`valmin`	−1 m	−2°C	−2°C	0 psu
`valmax`	1 m	32°C	32°C	36 psu
`valamax`	1 m	10°C	7°C	1 psu

$$|S^{\mathrm{a}} - S^{\mathrm{f}}| \leq 1, \quad 25 \leq S^{\mathrm{a}} \leq 36 \tag{13.33}$$

where T^{f} and S^{f} are the forecast values of the temperature and salinity, respectively.

13.2.7 Incremental Analysis Update

The analysis data estimated using an optimal interpolation scheme is generally used as the initial condition of the next forecast experiment (e.g., Mellor and Ezer 1991; Ezer and Mellor 1994). The estimated data, however, does not satisfy governing equations of the model because the optimal interpolation scheme doest not take account of them. Hence the forecast result might be infected by fictitious inertio-gravity waves. Mellor and Ezer (1991) modified the velocity field through a diagnostic calculation in such a way that it is geostrophically balanced with the density field based on the analysis data.

Another simple initialization scheme is nudging technique. In the scheme, the forecast data is continuously restored to the analysis data,

$$X^{n+1} = X^n + \frac{X^{\mathrm{a}} - X^n}{\tau_{\mathrm{nudge}}} \Delta t \tag{13.34}$$

where X^{n+1} and X^n are values of a variable at time level $n+1$ and n, respectively, X^{a} is an analysis value of the variable at an analysis time, τ_{nudge} is e-folding time scale during which the forecast value approaches to the analysis value, and Δt is the model time step. It is well known that the nudging scheme tends to impose more fictitious inertio-gravity waves on the model than the optimal interpolation scheme. Moreover the response of the model to the nudging, as shown in the end of this subsection, depends strongly upon the e-folding time scale.

In our forecast system we introduce, instead of the above schemes, an incremental analysis update (IAU) scheme (Bloom et al., 1996). The formulation is similar to the nudging scheme,

$$X^{n+1} = X^n + \frac{X^{\mathrm{a}} - X^{\mathrm{f}}}{\tau_{I\mathrm{AU}}} \Delta t \tag{13.35}$$

where X^{f} is a forecast data at the same analysis time as for X^{a} and $\tau_{I\mathrm{AU}} = 7$ days is a period of the IAU cycle. Equation (13.35) indicates that the analysis increments that are differences between the analysis and the forecast data are gradually incorporated into the model over the period. The increments are constants during each IAU cycle.

Figure 13.4 illustrates the flow of the IAU scheme. (1) A previous IAU cycle provides an initial condition of a forecast. (2) The forecast experiment is conducted for $\tau_{I\mathrm{AU}}/2$ (=3.5 days).[8] (3) The output data of the forecast process is provided to the

[8] The forecast experiment is, in fact, conducted for 60 days in each cycle as shown in Fig. 13.4 in order to provide the information about the Kuroshio path variation for public people. Miyazawa et al. (2005) suggest that the model has a predictability skill up to approximately 2 months for the variation.

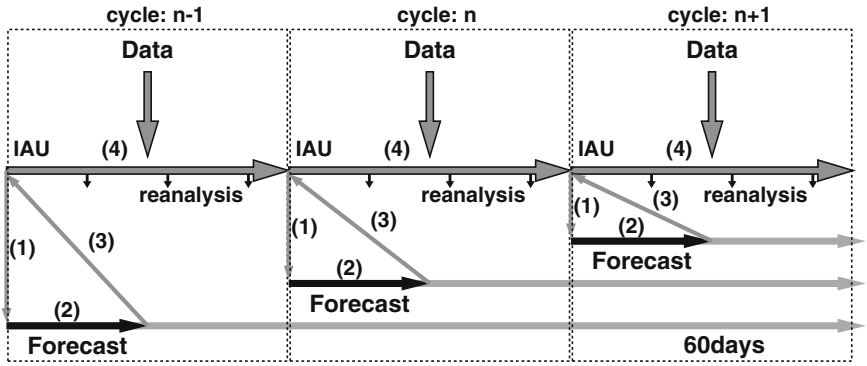

Fig. 13.4 Flow chart for the IAU and forecast. Numbers in the parentheses indicate the order of procedures

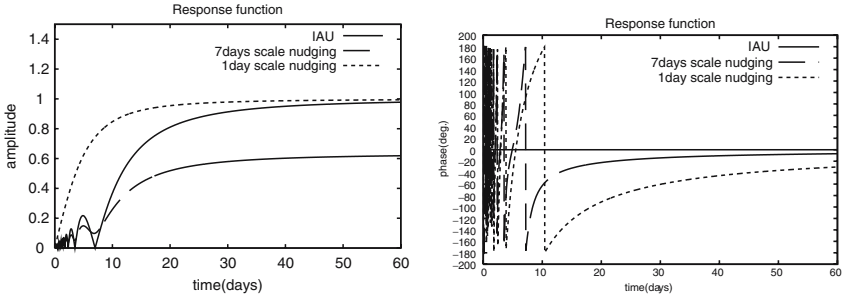

Fig. 13.5 Comparison of the amplitude (*left*) and phase (*right*) response of filters. *Solid*: The IAU with τ_{IAU}=7 days. *Dashed*: The nudging with τ_{nudge}=7 days. *Dotted*: The nudging with τ_{nudge}=1 day

IAU scheme, and the analysis increment is determined. (4) The increment is incorporated into the model by following (13.35). During a cycle of the IAU process, model results are stored at 2 days interval as shown in Fig. 13.4. We call these output the reanalysis. Then these procedures are continuously carried out.

Finally we will show the superiority of the IAU scheme to the nudging scheme. Assuming that the governing equations are linear, we can examine the response characteristics of the filters such as the IAU and the nudging (Bloom et al., 1996). After the IAU with τ_{IAU}=7 days is applied, phenomena on the 20 days time scale will lose 20% of their amplitude, but the decrease of the signal amplitude asymptotically approaches to zero as the time scale of phenomena gets longer (left panel of Fig. 13.5). Moreover the phase error is almost null for phenomena with time scale longer than 7 days (right panel of Fig. 13.5). On the other hand, although the phase error due to the nudging with the same time scale as the IAU is quite small, the amplitude response is terribly bad. Phenomena with the 60 days time scale will lose 40% of its amplitude because of the nudging. The nudging with the e-folding scale of

1 day is superior to the others in the amplitude response, but inferior in the phase response. This comparison implicates that the IAU is a better low-pass filter than the nudging.

13.3 Predictions of the Kuroshio Large Meander

We have carried out the forecast experiment of the Kuroshio large meander since December 2001. The forecast lead time is 2 months, which is determined in such a way that RMS errors of ensemble forecast experiments do not exceed the magnitude of the model climatic variation, and those obtained from nonassimilated simulations and persistence (Miyazawa et al., 2005). Forecast results and the reanalysis data described in the previous section are distributed from the web site `http://www.jamstec.go.jp/frsgc/jcope/`, and updated on every Saturday. In this section, we will take a couple of examples from the recent forecasts of the Kuroshio path variations. We will also describe the sensitivity of the July–October 2004 forecast to a couple of parameters used in the data assimilation scheme.

13.3.1 Case for April to June 2003

In April 2003 the Kuroshio took the nearshore nonlarge-meander path with a small offshore displacement south of the Kii Peninsula moving approximately 250 km east from south of Shikoku Island. On the offshore side of the Kuroshio south of the peninsula a westward surface current is evident between 30.5°N and 32.5°N, suggesting the existence of an anticyclonic eddy (upper left panel of Fig. 13.6). Existence of another small anticyclonic eddy around 140°E on the offshore side of the Kuroshio is also suggested.

The forecast model is initialized with the IAU output on April 26, 2003. The upper right panel of Fig. 13.6 shows a nowcast of the SSH, indicating that the Kuroshio flowing along the Japanese coast and the existence of two major anticyclonic eddies south of the Kii Peninsula are represented well.

In the May 2003 forecast (1-month lead time forecast), the model predicts the development of the offshore displacement (small meander) of the path southeast of the Kii Peninsula (middle right panel of Fig. 13.6), in perfect accord with the observation on its zonal and meridional extents: approximately 450 km and 250 km. In the meander, a cyclonic eddy is formed. On the onshore side of the eddy, the speed of the westward coastal current exceeds 0.5 $\mathrm{m\,s^{-1}}$ at places based on the one-time observation (middle left panel of Fig. 13.6), while that in the 2-day mean forecast is at most $0.25\,\mathrm{m\,s^{-1}}$. The underestimate is partly because the observation fields are instantaneous, and partly because the model needs more horizontal resolution to resolve such local phenomena.

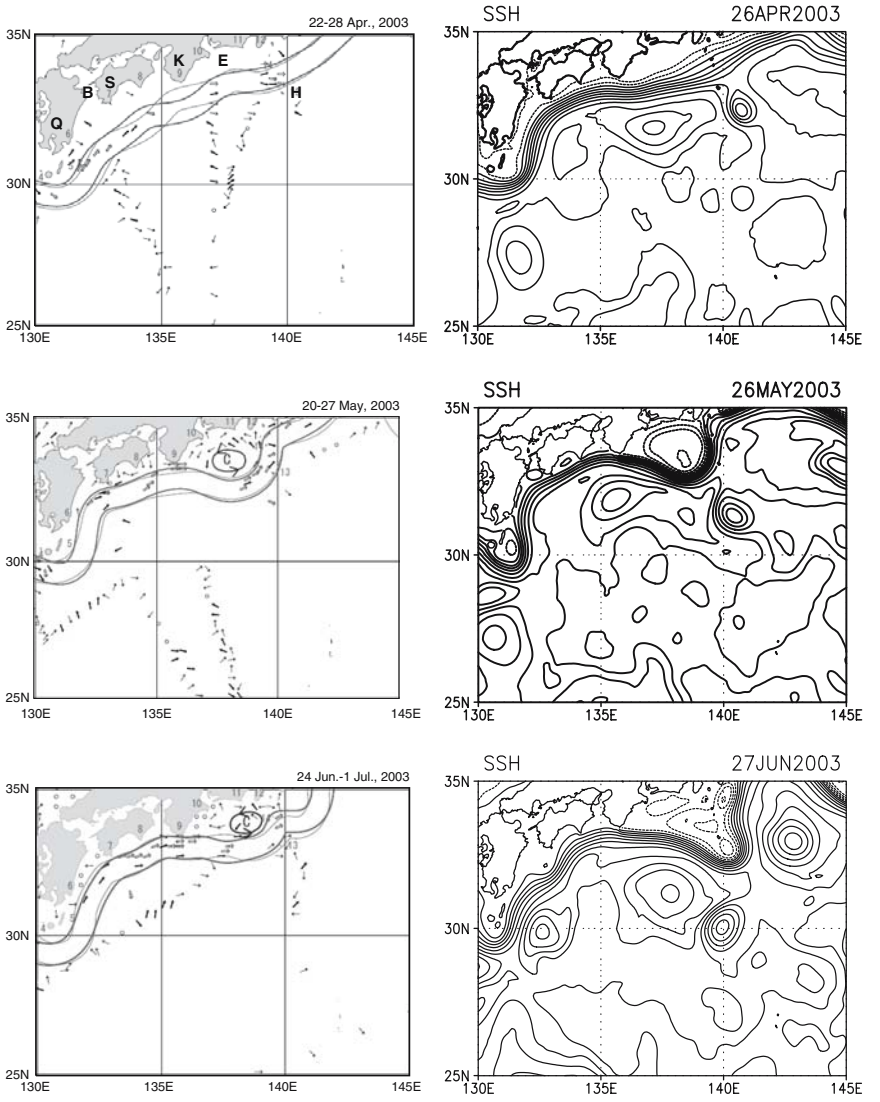

Fig. 13.6 *Left*: Weekly mean observed Kuroshio path during April 22, 2003 to July 1, 2003 reported in the Quick Bulletin Ocean Conditions provided by Hydrographic and Oceanographic Department, Japan Coastal Guard. The *thin line* delineates the Kuroshio path of a week ago and the thick is the current path. *Arrows* indicate the surface velocity at 0.15–0.5 m s^{-1} (*thin*), 0.5–1.0 m s^{-1} (*thick*) and 1.1–2.5 m s^{-1} (*open*). *Right*: Model SSH in 2-day mean of the forecast initialized on April 26, 2003. Contour interval is 0.05 m. Solid contours correspond to positive values of the SSH, and dotted contours to negative values. In the *upper left panel*, K, E, S, Q, H, and B denote the Kii Peninsula, Enshu-nada Sea, Shikoku, Kyushu, and Hachijo-jima Islands, and the Bungo Channel, respectively

In the June 2003 forecast (2-month lead time forecast), the small meander moves eastward, leading to the offshore nonlarge meander path, which is close to the observation, although the observed path is distorted in the W-shaped pattern (lower panels of Fig. 13.6). Furthermore, our forecast model initialized in the beginning of June predicts the subsequent eastward movement of the meander, eventually causing the Kuroshio to take the nearshore nonlarge meander path in the end of July (not shown). Note that the model seems to predict well the anticyclonic eddy southeast of Kyushu Island, which is barely perceptible from the spatially sparse observation (lower left panel of Fig. 13.6).

13.3.2 Case for May to July 2004

A small meander of the Kuroshio occurs southeast of Kyushu in the beginning of 2004 (not shown), stays there with growing its size until June 2004 (middle left panel of Fig. 13.7). It starts to move eastward slowly in the second week of June 2004, and grows into a large meander at the end of July 2004.

In 1-week lead time forecast initialized on May 1, 2004, the small meander moves to the east and its head reaches the south tip of the Kii Peninsula (upper right panel of Fig. 13.7), showing a pattern similar to the observation on June 1–8, 2004 or in a week before delineated by the thin line in the middle left panel of Fig. 13.7.

In the June 2004 forecast (1-month lead time forecast), the center of the meander reaches the south of the peninsula in a way similar to the observation in the end of July 2004. As the meander moves to the east, the anticyclonic eddies in the east and west of it develop (middle right panel of Fig. 13.7).

In the July 2004 forecast (2-month lead time forecast), the Kuroshio large meander reaches its mature state. The anticyclonic eddy east of the meander moves westward along the path and is merged into another, then the eddy west of the meander further develops (lower right panel of Fig. 13.7).

This is the first success in predicting the Kuroshio large meander as well as the occurrence of its triggering meander southeast of Kyushu Island (not shown) using both the numerical model and available observation data, although the model has a bias in the eastward movement speed of the small meander along the Japanese coast as described earlier. In the model the small triggering meander takes approximately 4 months to grow into the large meander after its appearance, while it does approximately 7 months in the real ocean. Previous hydrographic observations, however, indicate that the small meander usually takes approximately 4 months to grow into the large meander after its appearance southeast of Kyushu Island (Kawabe, 1986), suggesting that its eastward movement speed in the model is consistent with those in past events. This means that the model will perhaps be able to predict the path transition of the Kuroshio observed in the more past in a relatively accurate way compared with the 2004 forecast, but, at the same time that the model perhaps misses some mechanism to explain why the small meander takes approximately 7 months to grow into the large meander after its appearance.

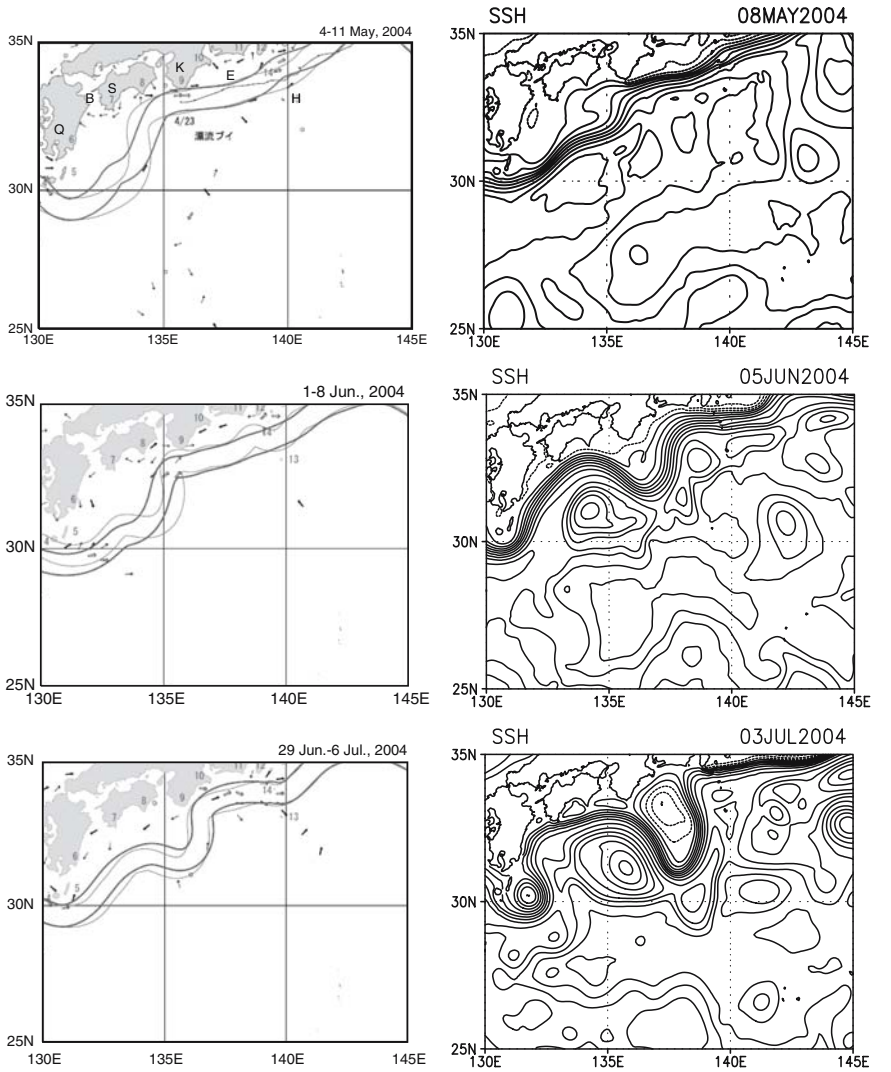

Fig. 13.7 Same as Fig. 13.6 except for the period during May 4, 2004 to July 6, 2004 and the forecast initialized on May 1, 2004

13.3.3 Sensitivity of the Forecast to Parameters

Since the forecast is quite sensitive to parameters used in the data assimilation scheme (Table 13.2), we have conducted lots of trial-and-error experiments in such a way that the forecast of the path transition of the Kuroshio that occurred in the past becomes reasonable. In this subsection, we will take an example to show how

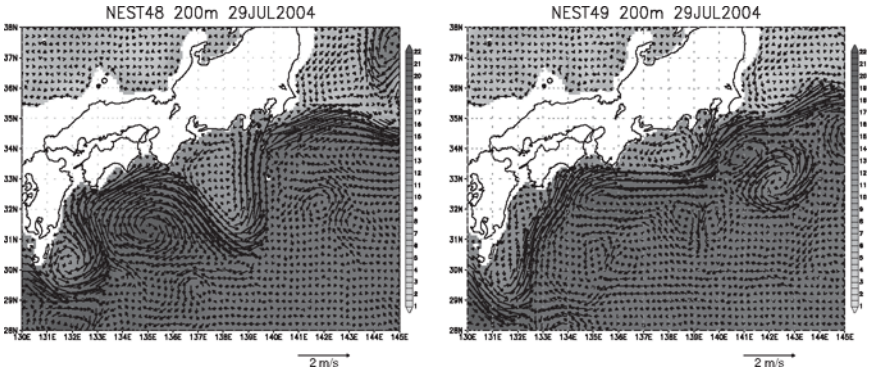

Fig. 13.8 Comparison of the 2-month lead time forecasts initialized on May 6, 2004 obtained with two different sets of parameters. Shading and vectors denote the temperature (°C) and velocity (m s^{-1}) at 200 m, respectively. *Left*: With parameters listed in Table 13.2. *Right*: Same as the left panel except that `vcorimps` and `vobsieadj` for the SSH are 1.0 and 0.01, respectively

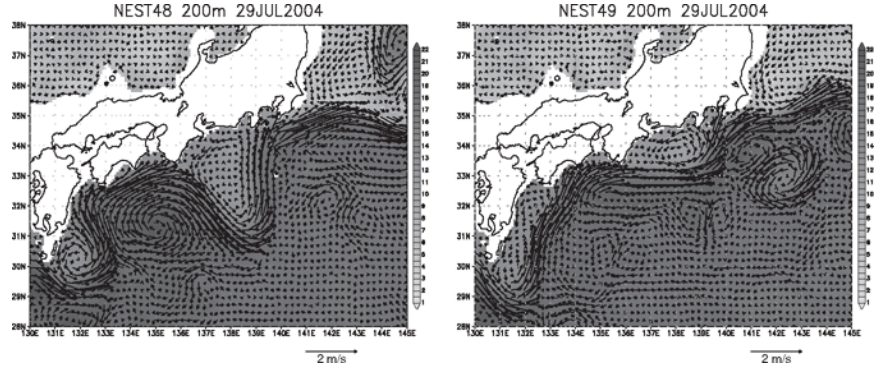

Fig. 13.9 Same as Fig. 13.8 except for the forecast initialized on June 3, 2004

sensitive the model is to a couple of parameters. The experiment with parameter values listed in Tables 13.2 and 13.3 is called the standard case, while that with the same values except for `vcorimps` and `vobsieadj` for the SSH is the test case. The former one is the adjustable parameter by which the regression coefficient between the salinity at the depth k and the SSH, and the latter is α'_η in (13.28).

The standard case shows that the large meander path is stable in a sense of its meridional extent, although the path slightly vibrates in the zonal direction (left panels of Figs. 13.8–13.11). On the other hand, in the test case where `vcorimps` and `vobsieadj` for the SSH are set to be 1.0 and 0.01, respectively, the meridional amplitude of the large meander changes drastically in a manner that depends upon the initialization date. These changes are mainly due to the detachment of anticyclonic eddies from the Kuroshio (right panel of Fig. 13.9). Numbers of pinched-off eddies suggest that the Kuroshio might be under the baroclinically unstable condition.

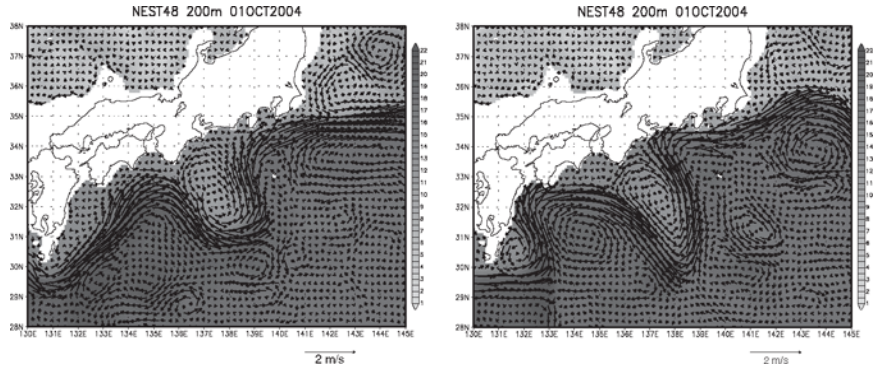

Fig. 13.10 Same as Fig. 13.8 except for the forecast initialized on July 1, 2004

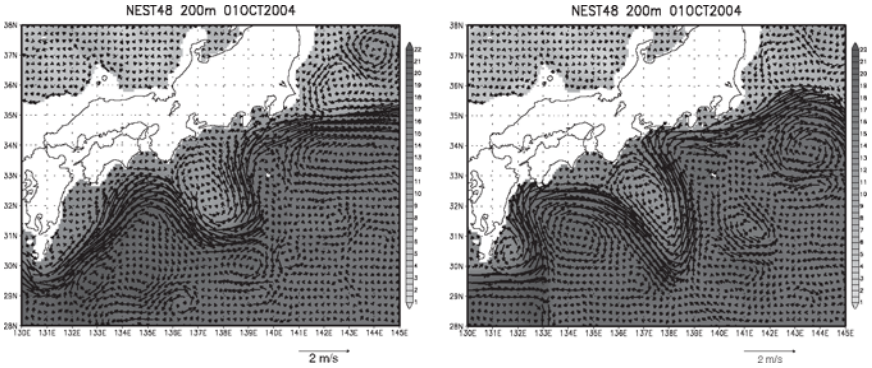

Fig. 13.11 Same as Fig. 13.8 except for the forecast initialized on August 6, 2004

The above example indicates that even a couple of parameters may drastically change a dynamical balance in the model, thus that a careful choice of the parameters is required in such a way that a reasonable forecast is accomplished. The parameters that we use for the operational forecast of the Kuroshio path variation are not perfect, but better at this moment. We still now explore the parameter sensitivity.

13.4 Toward the Kuroshio Forecast Downscaling for Coastal Oceans and Bays

As described in Introduction, the coastal waters around Japan are strongly influenced by the Kuroshio. The variation in its path such as the large meander has been well known to affect the water temperature in some semienclosed bays along the southern coast of Japan (Kawabe and Yoneno, 1987) and a biological state there (Nakata et al., 2000). Even during the period of the nearshore nonlarge meander path, a short-term variation in the Kuroshio also affects hydrographic conditions in the enclosed bays.

For example, it has been reported that an abnormally strong warm current (the Kyucho) originating from the Kuroshio intrudes into the Bungo Channel[9] (Takeoka et al. 1993) and the Sagami Bay (Uda 1953; Matsuyama and Iwata 1977), and results in a steep temperature rise there. Such local phenomena, however, cannot be resolved by the present Kuroshio forecast model described in the previous sections, thus we need to develop a further fine resolution forecast model for coastal oceans and bays south of Japan in order to understand and predict the influence of the Kuroshio on the coastal waters.

As the first step of such efforts, which are extensions of the present Kuroshio forecast system, we chose the Suruga Bay, Sagami Bay, and Tokyo Bay as our target areas (see Fig. 13.12). These bays are surrounded by many important industrial areas in Japan and several big cities such as Tokyo and Yokohama. As a research site for oceanography, they are one of the most active places in Japan. At present, in addition to the physical problems such as the Kyucho and internal tides, the primary production and the fisheries are also being deeply concerned, for which several big research projects have been released by the national and local governments and universities. Therefore, our modeling efforts will provide a framework for the future interdisciplinary researches.

In this section, we will introduce some results of a tidal simulation. Other simulations forced by either the geostrophic currents or the river runoff, or by all of them including the tides are still under way, and the results will be reported in other papers. We note that the basic idea beneath our activities is that the correct prediction of an oceanic current intrusion into a coastal water depends upon not only the correct open boundary conditions but also a good background field inside the coastal water. The former has been partly guaranteed by the present Kuroshio forecast system but the latter still needs more efforts.

The numerical model that we use for the tidal simulation is based on the two-dimensional version of the POM. The horizontal resolution is $1/108° \times 1/108°$ (approximately 0.854 km in the zonal and 1.031 km in the meridional direction). The bottom topography data with 500 m resolution archived by Hydrographic and Oceanographic Department, Japan Coastal Guard is used after smoothed out with the filter based on Mellor et al. (1994), as described in Sect. 13.2.1. The bottom drag coefficient is set to be a constant (=0.0026). The external forcing is only the barotropic tide listed in the Table 13.4. The tidal constants (amplitude and phase lag) for each tidal constituent are provided by Matsumoto et al.'s (2000) model output

Table 13.4 Four principal components of the tide used as the forcing

Abbreviation	Character	Period [h]
M_2	Principal lunar semidiurnal	12.4206
S_2	Principal solar semidiurnal	12.0000
O_1	Lunar diurnal	25.8193
K_1	Lunisolar diurnal	23.9345

[9] The location of the Bungo Channel is denoted by B in the upper left panel of Fig. 13.6.

with 1/12° resolution, into which the available harmonic constants obtained from the tide gauges around Japan and those over the open ocean calculated directly from TOPEX/POSEIDON altimetry are assimilated. The tide calculated with the spatially interpolated tidal constants is given at three lateral open boundaries, but the tidal potential forcing is not taken into account. The barotropic velocity normal to the open boundary is modified in the same way as described in Sect. 13.2.2 except that η_c in (13.2) is the tide, $c_{rf} = 1$ and $\bar{u}_c$ is the barotropic velocity at a grid inside the open boundary. The model is integrated for 7 days from a state of rest with the time step of 0.5 s, and the output from the last 2 days is used for harmonic tidal analysis.

Figures 13.12 and 13.13 show the corange and cotidal lines obtained from the model forced with M_2 and O_1 tides, respectively. Both tidal waves propagate from east to west. Whereas the amplitude of M_2 tide increases from east to west, that of O_1 tide from the offshore side to the onshore side, suggesting a boundary trapped wave. In fact O_1 tide does not have a feature of Poincaré wave, but that of Kelvin wave because its frequency ($=0.818f$) is less than the inertial frequency, f. Comparison between the tide gauge observation and the model result indicates that their differences with regard to both the amplitude and phase are within a reasonable range (the amplitude error of M_2 tide is less than 5% of the observed amplitude in most of places) at all observation points except for those around the Tokyo Bay. The large difference in the Tokyo Bay may be due to the lack of the horizontal resolution compared to the least width of the bay mouth (approximately 7 km).

The tidal current is generally parallel to the coast line, as shown by flat ellipses in Fig. 13.14. It is, however, intriguing that M_2 tidal current indicates an obvious

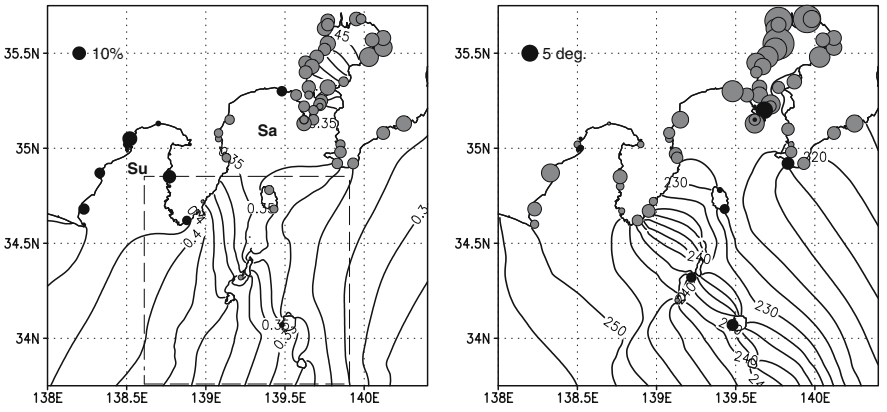

Fig. 13.12 Comparison of M_2 tide amplitude (*left*) and phase (*right*) between the model and observation based on the tide gauge. The area of circles is proportional to the difference between them. *Black (Gray) circles* indicates that the model amplitude is larger (smaller) than the observation, and that the model (observation) lags the observation (model). *Contour lines* delineate the corange in m (left) and cotide in degree (right) obtained from the model. Contour interval is 0.01 m for corange and 2°for cotide. Su and Sa denote Suruga Bay and Sagami Bay, respectively. *Dashed line* denotes the area in which the tidal ellipse is delineated (Fig. 13.14)

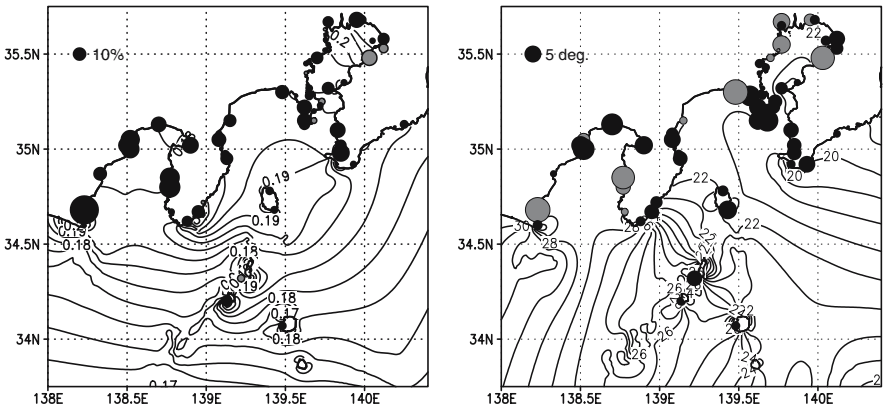

Fig. 13.13 Same as Fig. 13.12 except for the O_1 tide. Contour interval is 0.002 m for corange and 0.5° for cotide

clockwise rotation over the Izu-Ogasawara Ridge, particularly near the Izu Islands, whereas the tidal current rotates anticlockwise in the south of Japan apart from the ridge (not shown). Although the observed basic features of the tidal current are represented well in the model, the tidal current speed is underestimated particularly in the head of Sagami Bay and Suruga Bay. This is because of the presence of strong internal tide in these bays (Ohwaki et al. 1991; Takeuchi and Hibiya 1997). At present, we have finished simulations of the internal tide and confirmed the reproduction of the observed strong tidal currents in Sagami Bay and Suruga Bay with the use of our coastal model. Readers can refer to Kawajiri et al. (2006) for the details about the reproduction of internal tide as well as other aspects of the tidal simulation such as effects of tidal potential forcing, problems related to the open boundary conditions, and an interaction between four tidal constituents listed in Table 13.4.

13.5 Summary

We have described the detail of the Kuroshio forecast system with approximately 10 km resolution, called the JCOPE (Japan Coastal Ocean Predictability Experiment) ocean forecast system, specifically with regard to the spatio-temporal interpolation of the observation data and the data assimilation technique including the incremental analysis update scheme. Although the system is, as described in Sect. 13.3.3, not perfect particularly in a sense of parameter setting, we believe that this documentation is useful for readers to develop an ocean forecast system.

Two examples of the prediction of the Kuroshio path variations using the system are introduced. The system successfully predicts the path transitions from the nearshore nonlarge meander path to the offshore nonlarge meander path in 2003, and

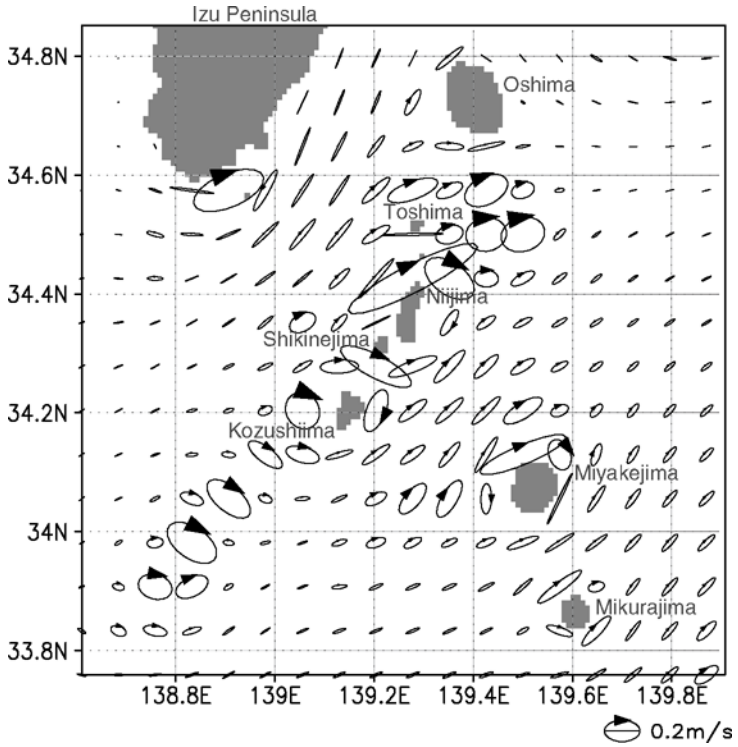

Fig. 13.14 M_2 tidal current ellipses around the Izu Islands

from the nearshore nonlarge meander path to the typical large meander path in 2004 as well as the occurrence of its triggering small meander south of Kyushu Island. Note that the success of the 2004 forecast is attributed to the recent establishment of observation network (satellites, ships, and ARGO floats) as well as the sophistication of both the numerical model and the data assimilation technique, suggesting that they are just like the wheels of a car. We also note that it enables us to deeply understand how the path transitions of the Kuroshio occur.

For the purpose of the Kuroshio forecast downscaling for coastal oceans and bay areas, we have, for the first step, conducted the tidal simulation with a state-of-the-art model. Comparison between the tide gauge observation and the model result indicates that their differences with regard to both amplitude and phase are within a reasonable range. It is quite intriguing that M_2 tidal current rotates clockwise only over the Izu-Ogasawara Ridge in our analysis area. Moreover the strong tidal current at that place, particularly near the Kuroshio path, suggests its nonlinear interaction with the Kuroshio. It is, however, out of the scope of this manuscript, hence we leave them as future subjects.

More accurate forecasts require further reduction of model biases shown in Sect. 13.3. Comparing the JCOPE reanalysis data and the individual hydrographic

observation that are not assimilated into the model, we realize that the model temperature tends to have a positive bias in the onshore side of the Kuroshio and a negative bias in the upper 50 m and the thermocline layer of its offshore side. The representation of the density field particularly in the onshore side of the Kuroshio is very crucial in predicting the path transition of the Kuroshio accurately, because the eastward movement and development of the small trigger meander are related to the baroclinic instability. Hence we have been investigating causes of the biases through numerous sensitivity experiments to parameters and numerical schemes, and also developing, on the basis of Hukuda and Guo (2004), a two-way nesting forecast model which consists of the current fine model and a regional model for the Kuroshio area with 1/36°resolution and thereby may represent a sharp density front in the onshore side of the Kuroshio more accurately than the current model.

Outputs of the current JCOPE ocean forecast system can be utilized as pseudo-data for many purposes. Because of the fineness of the horizontal resolution, the JCOPE reanalysis data have been used for the lateral boundary condition of a regional ocean model (e.g., Suzuki et al. 2004; Uchimoto et al. 2006) and for the bottom boundary condition of a regional atmospheric model (e.g., Yamaguchi et al. 2005). In the latter case, the short-term variations of the rainfall and surface wind associated with the typhoon passing are represented consistently with the observation by a hindcast experiment with the SST obtained from the JCOPE model compared to another experiment with the surface skin temperature from NCEP Global Forecast System, suggesting that the predicted SST by the JCOPE system may be useful to local severe weather forecasting and notification. Recently the Fisheries Research Agency has started to investigate dispersal of eggs and larvae of anchovy and horse mackerel using the velocity field of the JCOPE reanalysis data to attain the goal of evaluating fisheries resources and predicting fishing grounds. The JAMSTEC has tentatively utilized the velocity data for the operation of the Deep Sea Drilling Vessels “CHIKYU” because the strong current has a particularly serious impact on the ability of a drilling rig to maintain its position. We expect that the JCOPE ocean forecast system may contribute to as many societies as possible because of its wide availability.

Acknowledgments We are greatly indebted to Prof. Toshio Yamagata and Dr. Hirofumi Sakuma for their encouragement and the management of our research activity. The JCOPE project is supported by the Frontier Research Center for Global Change/JAMSTEC. The QuikSCAT data is obtained from the NASA/NOAA sponsored data system Seaflux, at JPL through the courtesy of Dr. W. Timothy Liu and Dr. Wenqing Tang. The comparison study between the JCOPE output and the hydrographic data and the sensitivity study are supported by Dr. Kosei Komatsu, Dr. Takashi Setou, and many collaborators in the Fisheries Research Agency.

References

Akitomo, K., T. Awaji, and N. Imasato, 1991: Kuroshio path variation south of Japan 1. Barotropic inflow-outflow model. *J. Geophys. Res.*, **96**, 2549–2560.

Akitomo, K. and M. Kurogi, 2001: Path transition of the Kuroshio due to mesoscale eddies: A two-layer, wind-driven experiment. *J. Oceanogr.*, **57**, 735–741.

Bloom, S. C., L. L. Takacs, A. M. da Silva, and D. Ledvina, 1996: Data assimilation using Increment Analysis Updates. *Mon. Wea. Rev.*, **124**, 1256–1271.

Boyer, T. P. and S. Levitus, 1997: Objective Analyses of Temperature and Salinity for the World Ocean on a 1/4° Grid. Noaa/nesdis atlas 11, U.S. Gov. Printing Office, Washington, D.C.

Bryden, H. L., D. H. Roemmich, and J. A. Church, 1991: Ocean heat transport across 24°N in the Pacific. *Deep-Sea Res.*, **38**, 297–324.

Ebuchi, N. and K. Hanawa, 2000: Mesoscale eddies observed by TOLEX-ADCP and TOPEX/POSEIDON altimeter in the Kuroshio recirculation region south of Japan. *J. Oceanogr.*, **56**, 43–57.

Endoh, T. and T. Hibiya, 2000: Numerical study of the generation and propagation of trigger meanders of the Kuroshio south of Japan. *J. Oceanogr.*, **56**, 409–418.

Ezer, T., 2000: On the seasonal mixed layer simulated by a basin-scale ocean model and the Mellor-Yamada turbulence scheme. *J. Geophys. Res.*, **105**, 16843–16855.

Ezer, T. and G. L. Mellor, 1994: Continuous assimilation of Geosat altimeter data into a three-dimensional primitive equation Gulf Stream model. *J. Phys. Oceanogr.*, **24**, 832–847.

— 1997: Data assimilation experiments in the Gulf Stream region: How useful are satellite-derived surface data for nowcasting the subsurface fields? *J. Atmos. Oceanic Technol.*, **14**, 1379–1391.

— 2004: A generalized coordinate ocean model and a comparison of the bottom boundary layer dynamics in terrain-following and in z-level grids. *Ocean Model.*, **6**, 379–403.

Flather, R. A., 1976: A tidal model of the northwest European continental shelf. *Memories da la Societe Roylale des Sicences de Liege*, **6**, 141–164.

Fox, A. D., K. Haines, B. A. de Cuevas, and D. J. Webb, 2000: Altimeter assimilation in the OCCAM global model Part II: TOPEX/POSEIDON and ERS-1 assimilation. *J. Mar. Systems*, **26**, 323–347.

Gandin, L. S., 1963: Objective analysis of meteorological field. Gidrometeorologicheskoe Izdate'stvo., 287 pp.

Guo, X., H. Hukuda, Y. Miyazawa, and T. Yamagata, 2003: A triply nested ocean models – Roles of horizontal resolution on JEBAR. *J. Phys. Oceanogr.*, **33**, 146–169.

Hinata, H., T. Yanagi, T. Takao, and H. Kawamura, 2005: Wind-induced Kuroshio warm water intrusion into Sagami Bay. *J. Geophys. Res.*, **110**, doi:10.1029/2004JC002300.

Hukuda, H. and X. Guo, 2004: Application of a two-way nested model to the seamount problem. *J. Oceanogr.*, **60**, 893–904.

Hurlburt, H. E., A. J. Wallcraft, W. J. Schmitz, Jr., P. J. Hogan, and E. J. Metzger, 1996: Dynamics of the Kuroshio/Oyashio current system using eddy-resolving models of the North Pacific Ocean. *J. Geophys. Res.*, **101**, 941–976.

Ichikawa, H. and M. Chaen, 2000: Seasonal variation of heat and freshwater transports by the Kuroshio in the East China Sea. *J. Mar. Systems*, **24**, 119–129.

Ichikawa, K. and S. Imawaki, 1994: Life history of a cyclonic ring detached from the Kuroshio Extension as seen by the Geosat altimeter. *J. Geophys. Res.*, **99**, 15953–15966.

Inatsu, M., H. Mukougawa, and S.-P. Xie, 2002: Tropical and extratropical SST effects on the midlatitude storm track. *J. Meteor. Soc. Jpn.*, **80**, 1069–1076.

Ishikawa, Y., T. Awaji, N. Komori, and T. Toyoda, 2004: Application of sensitivity analysis using an adjoint model for short-range forecasts of the Kuroshio path south of Japan. *J. Oceanogr.*, **60**, 293–301.

Iwata, S. and M. Matsuyama, 1989: Surface circulation in Sagami Bay: The response to variations of the Kuroshio axis. *J. Oceanogr. Soc. Jpn.*, **45**, 310–320.

Jerlov, N. G., 1976: Marine Optics. Elsevier Sci. Pub. Co., Amsterdam, 231 pp.

Kagimoto, T.: 2003, Sensitivity of the Equatorial Undercurrent to the vertical mixing parameterization. *Proc. 2003 Terrain-Following Ocean Models Users Workshop in Seattle*, available from `http://www.aos.princeton.edu/WWWPUBLIC/htdocs.pom/SIG03/SEATTLE03.pdf`.

Kagimoto, T. and T. Yamagata, 1997: Seasonal transport variations of the Kuroshio: An OGCM simulation. *J. Phys. Oceanogr.*, **27**, 403–418.

Kalnay, E., M. Kanamitsu, R. Kistler, W. Collins, D. Deaven, L. Gandin, M. Iredell, S. Saha, G. White, J. Woollen, Y. Zhu, M. Chelliah, W. Ebisuzaki, W. Higgins, J. Janowiak, K. C. Mo,

C. Ropelewski, J. Wang, A. Leetmaa, R. Reynolds, R. Jenne, and D. Joseph, 1996: The NCEP/NCAR 40-Year Reanalysis Project. *Bull. Am. Meteorol. Soc.*, **77**, 437–471.

Kamachi, M., T. Kuragano, H. Ichikawa, H. Nakamura, A. Nishina, A. Isobe, D. Ambe, M. Arai, N. Gohda, S. Sugimoto, K. Yoshita, T. Sakurai, and F. Uboldi, 2004a: Operational data assimilation system for the Kuroshio south of Japan: Reanalysis and validation. *J. Oceanogr.*, **60**, 303–312.

Kamachi, M., T. Kuragano, S. Sugimoto, K. Yoshita, T. Sakurai, T. Nakano, N. Usui, and F. Uboldi, 2004b: Short-range prediction experiments with operational data assimilation system for the Kuroshio south of Japan. *J. Oceanogr.*, **60**, 269–282.

Kawabe, M., 1986: Transition processes between the three typical paths of the Kuroshio. *J. Oceanogr. Soc. Jpn.*, **41**, 307–326.

Kawabe, M. and M. Yoneno, 1987: Water and flow variations in Sagami Bay under the influence of the Kuroshio path. *J. Oceanogr. Soc. Jpn.*, **43**, 283–294.

Kawajiri, H., X. Guo, T. Kagimoto, and Y. Miyazawa. Simulations of barotropic and baroclinic tides in coastal waters south of Tokyo, Japan. *J. Geophys. Res.*, (to be submitted).

Komori, N., T. Awaji, Y. Ishikawa, and T. Kuragano 2003: Short-range forecast experiments of the Kuroshio path variabilities south of Japan using TOPEX/Poseidon altimetric data. *J. Geophys. Res.*, **108**, doi:10.1029/2001JC001282.

Kondo, J., 1975: Air-sea bulk transfer coefficients in diabatic conditions. *Boundary-Layer Meteorol.*, **9**, 91–112.

Kuragano, T. and A. Shibata, 1997: Sea surface dynamic height of the Pacific Ocean derived from TOPEX/POSEIDON altimeter data: Calculation method and accuracy. *J. Oceanogr.*, **53**, 585–599.

Large, W. G. and S. Pond, 1981: Open ocean momentum flux measurements in moderate and strong winds. *J. Phys. Oceanogr.*, **11**, 324–336.

Levitus, S. and T. P. Boyer, 1994: World Ocean Atlas 1994, Volume 4: Temperature. Noaa atlas nesdis 4, U.S. Gov. Printing Office, Washington, D.C.

Levitus, S., R. Burgett, and T. P. Boyer, 1994: World Ocean Atlas 1994, Volume 3: Salinity. Noaa atlas nesdis 3, U.S. Gov. Printing Office, Washington, D.C.

Liu, W. T., W. Tang, and P. S. Polito, 1998: NASA scatterometer global ocean-surface wind fields with more structures than numerical weather prediction. *Geophys. Res. Lett.*, **25**, 761–764.

Lorenc, A. C., 1981: A global three-dimensional multivariate statistical interpolation scheme. *Mon. Wea. Rev.*, **109**, 701–721.

Lupton, R., 1993: Statistics in Theory and Practice. Princeton University Press, 188 pp.

Matsumoto, K., T. Takanezawa, and M. Ooe, 2000: Ocean tide models developed by assimilating TOPEX/POSEIDON altimeter data into hydrodynamical model: A global model and a regional model around Japan. *J. Oceanogr.*, **56**, 567–581.

Matsuyama, M. and S. Iwata, 1977: The Kyucho in Sagami Bay (I). *Bull. Fisheries Oceanogr. Jpn.*, **30**, 1–7, (in Japanese with English abstract).

Mellor, G. L., 2001: One-dimensional, ocean surface layer modeling, a problem and a solution. *J. Phys. Oceanogr.*, **31**, 790–809.

Mellor, G. L. and T. Ezer, 1991: A Gulf Stream model and an altimetry assimilation scheme. *J. Geophys. Res.*, **96**, 8779–8795.

Mellor, G. L., T. Ezer, and L.-Y. Oey, 1994: The pressure gradient conundrum of sigma coordinate ocean models. *J. Atmos. Oceanic Technol.*, **11**, 1126–1134.

Mellor, G. L., S. Häkkinen, T. Ezer, and R. Patchen: 2002, A generalization of a sigma coordinate ocean model and an intercomparison of model vertical grids. *Ocean Forecasting: Conceptual Basis and Applications*, N. Pinardi and J. D. Woods, eds., Springer, New York, 55–72.

Mellor, G. L. and T. Yamada, 1982: Development of a turbulence closure model for geophysical fluid problem. *Rev. Geophys. Space Phys.*, **20**, 851–875.

Menard, R. and L.-P. Chang, 2000: Assimilation of stratospheric chemical tracer observations using Kalman filter Part II: χ^2-validated results and analysis of variance and correlation dynamics. *Mon. Wea. Rev.*, **128**, 2672–2686.

Mitsudera, H., T. Waseda, Y. Yoshikawa, and B. Taguchi, 2001: Anticyclonic eddies and Kuroshio meander formation. *Geophys. Res. Lett.*, **28**, 2025–2028.

Miyazawa, Y., X. Guo, and T. Yamagata, 2004: Roles of meso-scale eddies in the Kuroshio paths. *J. Phys. Oceanogr.*, **34**, 2203–2222.

Miyazawa, Y., S. Yamane, X. Guo, and T. Yamagata, 2005: Ensemble forecast of the Kuroshio meandering. *J. Geophys. Res.*, **110**, doi:doi:10.1029/2004JC002426, doi:10.1029/2004JC002426.

Nakata, H., S. Funakoshi, and M. Nakamura, 2000: Alternating dominance of postlarval sardine and anchovy caught by coastal fishery in relation to the Kuroshio meander in the Enshu-nada Sea. *Fish. Oceanogr.*, **9**, 248–258.

Nonaka, M. and S.-P. Xie, 2003: Covariations of sea surface temperature and wind over the Kuroshio and its Extension: Evidence for ocean-to-atmosphere feedback. *J. Clim.*, **16**, 1404–1413.

Ohwaki, A., M. Matsuyama, and S. Iwata, 1991: Evidence for predominance of internal tidal currents in Sagami and Suruga Bays. *J. Oceanogr. Soc. Jpn.*, **47**, 194–206.

Paulson, E. A. and J. J. Simpson, 1977: Irradiance measurements in the upper ocean. *J. Phys. Oceanogr.*, **7**, 952–956.

Qiu, B. and K. A. Kelly, 1993: Upper-ocean heat balance in the Kuroshio Extension region. *J. Phys. Oceanogr.*, **23**, 2027–2041.

Qiu, B. and W. Miao, 2000: Kuroshio path variations south of Japan: Bimodality as a self-sustained internal oscillation. *J. Phys. Oceanogr.*, **30**, 2124–2137.

Reed, R. K., 1977: On estimating insolation over the ocean. *J. Phys. Oceanogr.*, **7**, 482–485.

Smagorinsky, J., 1963: General circulation experiments with the primitive equations. I. The basic experiment. *Mon. Wea. Rev.*, **91**, 99–164.

Suzuki, Y., K. Nadaoka, Y. Miyazawa, S. Harii, and N. Yasuda, 2004: Analysis of long-distance larval dispersal of corals and crow-of-thorns starfish using JCOPE and a coastal current model. *Ann. J. Coastal Eng., Jpn. Soc. Civil Eng.*, **51**, 1146–1150, (in Japanese).

Takeoka, H., H. Akiyama, and T. Kikuchi, 1993: The Kyucho in the Bungo Channel, Japan-periodic intrusion of oceanic warm water. *J. Oceanogr.*, **49**, 57–70.

Takeuchi, K. and T. Hibiya, 1997: Numerical simulation of baroclinic tidal currents in Suruga Bay and Uchiura Bay using a high resolution level model. *J. Oceanogr.*, **53**, 539–552.

Tetens, O., 1930: Über einige meteorologische Begriffe. *Z. Geophys.*, **6**, 293–309.

Uchimoto, K., H. Mitsudera, N. Ebuchi, and Y. Miyazawa, 2007: Anticyclonic eddy caused by the Soya Warm Current in an Okhotsk OGCM. *J. Oceanogr.*, **63**, 379–391.

Uda, M., 1953: On the stormy current (Kyucho) and its prediction in the Sagami Bay. *J. Oceanogr. Soc. Jpn.*, **9**, 15–22, (in Japanese with English abstract).

Yamaguchi, K., T. Yamashita, and K.-O. Kim, 2005. Effects of Kuroshio Warm Current SST on coastal wind and precipitation fields simulated by meso-scale meteorological model MM5. *Ann. J. Coastal Eng., Jpn. Soc. Civil Eng.*, **52**, 366–370 (in Japanese).